Reactivity Trends in the Gas Phase Addition of Acetylene to *N*-protonated Aryl Radical Cations

Oisin J. Shiels[†], P. D. Kelly[†], Cameron C. Bright[†], Berwyck L. J. Poad[‡], Stephen J. Blanksby[‡], Gabriel da Silva[¶], and Adam J. Trevitt*[†]

† Molecular Horizons and School of Chemistry and Molecular Bioscience, University of Wollongong, Wollongong, Australia, 2522 ‡ Central Analytical Research Facility, Institute for Future Environments, Queensland University of Technology, Brisbane, Australia, 4001 ¶ Department of Chemical Engineering, The University of Melbourne, Melbourne, Victoria, Australia, 3010

ABSTRACT: A key step in gas-phase polycyclic aromatic hydrocarbon (PAH) formation involves the addition of acetylene (or other alkyne) to σ-type aromatic radicals, with successive additions yielding more complex PAHs. A similar process can happen for N-containing aromatics. In cold diffuse environments, such as the interstellar medium, rates of radical addition may be enhanced when the σ-type radical is charged. This paper investigates the gas-phase ion-molecule reactions of acetylene with nine aromatic distonic σ-type radical cations derived from pyridinium (Pyr), anilinium (Anl) and benzonitrilium (Bzn) ions. Three isomers are studied in each case (radical sites at the *ortho, meta* and *para* positions). Using a room temperature ion trap, second-order rate coefficients, product branching ratios and reaction efficiencies are reported. The rate coefficients increase from *para* to *ortho* positions. The second-order rate coefficients can be sorted into three groups; low: between $1–3 \times 10^{-12}$ cm^3 molecule^{-1} s^{-1} (3Anl and 4Anl), intermediate: between $5–15 \times 10^{-12}$ cm^3 molecule^{-1} s^{-1} (2Bzn, 3Bzn and 4Bzn) and high: between $8–31 \times 10^{-11}$ cm^3 molecule^{-1} s^{-1} (2Anl, 2Pyr, 3Pyr and 4Pyr), and 2Anl is the only radical cation with a rate coefficient distinctly different to its isomers. Quantum chemical calculations, using M06-2X-D3(0)/6-31++G(2df,p) geometries and DSD-PBEP86-NL/aug-cc-pVQZ energies are deployed to rationalize reactivity trends based on the stability of pre-reactive complexes. The G3X-K method guides the assignment of product ions following formation of the adduct complexes. The rate coefficient trend can be rationalised by a simple model based on the pre-reactive complex forward barrier height.

Introduction

Ion-molecule reactions are involved in a variety of low-pressure gas-phase systems, ranging from Earth's atmosphere,[1] combustion[2-3] and the interstellar medium.[4-5] Due to long-range interactions between ions and neutral co-reactants, ion-molecule reactions generally possess larger collision cross-section values compared to their neutral counterparts. This makes them an important reaction class, particularly in low pressure and low temperature environments. Furthermore, gas-phase ion-molecule reactions can often exhibit negative temperature dependence (*i.e.*, increased reaction efficiency with lower temperature)[6-7] thus reinforcing their importance in low temperature and pressure environments of the interstellar medium and extra-terrestrial atmospheres such as Titan.

For ion-molecule reactions, the interplay between long-range and short-range interactions manifests in multistep energy pathways that influence the reaction rate and product yield(s). This is captured in the double-well potential energy model developed by Olmstead and Brauman and widely adopted to rationalise ion-molecule reactions.[8-10] This model accounts for the variations in gas-phase reaction rates for a variety of highly exothermic, S$_N$2 reaction archetypes. The double-well feature in the potential energy landscape is now generally accepted to be common to many classes of ion-molecule reactions to take into account the long-range attractive potentials and stabilised pre-reactive complexes.[11]

For gas phase ion-molecule reactions involving radical ions – particularly for distonic radical ions,[12-14] where radical and charge sites are spatially and electronically separated – several models have been developed to explain kinetic trends for reactions with neutral molecules. A well-developed concept is the ionic curve crossing model first proposed by Anderson *et al*.[15] based on modification of the earlier model of covalent curve-crossing.[16] This paradigm defines the barrier height of a polar radical-molecule reaction as an avoided crossing of the ground state and an ionic excited state potential. This model has been successfully applied to a number of radical H-atom abstractions including those involving distonic radical ions with σ-type aromatic radical sites.[14,17-19] However, other distonic reactions proceeding by addition/elimination mechanisms have not been as extensively examined using this generalised framework.

In the current study, three sets of protonated σ-type aromatic radicals have been prepared based on the dehydropyridinium, dehydroanilinium and dehydrobenzonitrilium cations (Figure 1). The gas phase reactions of each set of regioisomers – nine in total – with acetylene were studied. Each set contains three isomeric distonic radical cations, where the σ-radical is located at either the *ortho*, *meta* or *para* position with respect to the charged moiety. For each reaction, second-order rate coefficients and product branching ratios are measured and compared with quantum chemical calculations to assign

1

potential products and predict the reaction feasibility under low-temperature conditions. From kinetic measurements, a correlation between second-order rate coefficients and pre-reactive complex forward barrier heights is identified.
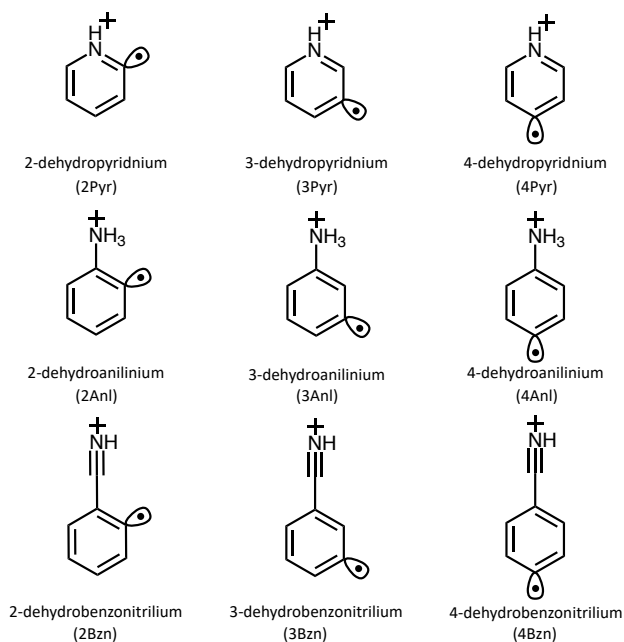

Figure 1. The nine distonic radical cations investigated in this study.

Methods

Instrumental

All reactions were performed using a linear quadrupole ion-trap mass spectrometer (Thermo Scientific LTQ XL), which has been modified as described previously.[20] The mass spectrometer was modified to include an alternative gas supply, bypassing the standard gas inlet. These modifications allow for the addition of neutral acetylene seeded within the helium buffer gas into the ion-trap region of the mass spectrometer. Gas flow through the alternative gas supply was regulated by a mass flow controller (MKS GE50A, 5 sccm) set to 1.300 sccm, which was allowed to flow for at least 12 h prior to kinetic measurements to ensure ion trap pressure and gas composition equilibrium. Additionally, a vacuum-sealed quartz window was positioned at the rear of the instrument chamber to allow laser access along the long axis of the linear ion trap. This window permitted the irradiation of stored ions by an external 266 nm Nd:YAG laser source (Continuum Minilite) that was pulsed once per mass spectrometry cycle.

Target radical cations were generated by 266 nm laser photolysis of protonated iodinated precursors within the ion trap. Iodinated precursor ions were formed by electrospray ionisation (ESI) of ~10 µM methanolic solutions of 2-iodoaniline (98%, Sigma-Aldrich), 3-iodoaniline (98%, Sigma-Aldrich), 4-iodoaniline (98%, Sigma-Aldrich), 2-iodopyridine (98%, Sigma-Aldrich), 3-iodopyridine (98%, Sigma-Aldrich), 4-iodopyridine (97%, Sigma-Aldrich), 2-iodobenzonitrile (98%, Sigma-Aldrich), 3-iodobenzonitrile (98%, Sigma-Aldrich) or 4-iodobenzonitrile (98%, Sigma-Aldrich). Sample solutions were introduced to the ESI source operating in positive ion mode using a flow rate of 5 µL min^{-1}. An acetylene and helium specialty mixture (BOC, NSW), doped with ~2% acetone relative to acetylene, was used as the source of the acetylene co-reactant. Acetone, present in the acetylene as a stabiliser, was removed using the sulfuric acid trap method, as described by Hyman and Arp.[21] A glycol pre-condenser was added to the purification set-up prior to acetylene collection, to eliminate the water by-product introduced by the acid trap. Purified acetylene was stored in stainless steel tanks and diluted in helium (0.1-1% acetylene).

Radical precursor ions [P + H]$^+$ were isolated and then stored for 30 ms within the ion trap and exposed to a single 266 nm laser pulse, leading to the formation of the target [P + H - I]$^{\bullet+}$ distonic radical cation through photolysis of the aryl-iodine bond. Once isolated and stored, radical cations were allowed to react with neutral reagents over time scales ranging from 0.03 – 5000 ms. Individual product mass spectra are reported as averages of no less than 75 scans. Across all reactions, acetylene number densities vastly exceeded those of the ions ensuring *pseudo*-first-order conditions with respect to acetylene. Kinetic data were obtained by integrating target *m/z* peaks (over a 1 Th range), which were normalised to the total ion signal (spanning *m/z* 50 – 300) and plotted against reaction time. *Pseudo*-first-order rate coefficients were extracted from these data by fitting either a single or biexponential function, using the Levenberg-Marquardt algorithm[22] and data points were weighted by their 95% confidence interval values. Extracted first-order rate coefficients were plotted against corresponding acetylene number density and fitted using linear regression to derive the second-order rate coefficient for each reaction. Reaction efficiencies (Φ) were calculated by dividing the measured second-order rate coefficients by the estimated Langevin collision rate.[23] Uncertainty in the pressure at the centre of the ion trap introduces a bound of ±50% in the absolute reaction efficiencies and second-order rate coefficients.[24] Internally, reaction rate coefficients have a precision on the order of 5-10%.

Computational

Structures and relative energies for minima, transition states and intrinsic reaction coordinate (IRC) scans were calculated using Gaussian 16. Initial calculations used the M06-2X functional [25] and 6-31G(2df,p) basis set. Pre-reactive complexes were recalculated using M06-2X-D3(0)/6-31++G(2df,p) geometries and DSD-PBEP86-NL/aug-cc-pVQZ energies to better capture long-range charge and electron interactions originating from non-covalent bonding of these complexes.[26] The DSD-PBEP86-NL functional is a double hybrid specifically designed and benchmarked to accurately calculate transition and minimum structures involving such long-range interactions.[27] Calculations for post-addition potential energy schemes were recalculated using the composite G3X-K method, which is designed and benchmarked for accurate transition state energy determination.[28] Minima were assigned as stationary points possessing no imaginary frequencies, while transition states were assigned as stationary points with exactly one imaginary frequency whose normal mode projection approximates motion along the reaction coordinate. All 0 K energies include the unscaled zero-point vibrational energy (ZPE) correction and are reported in kcal/mol.
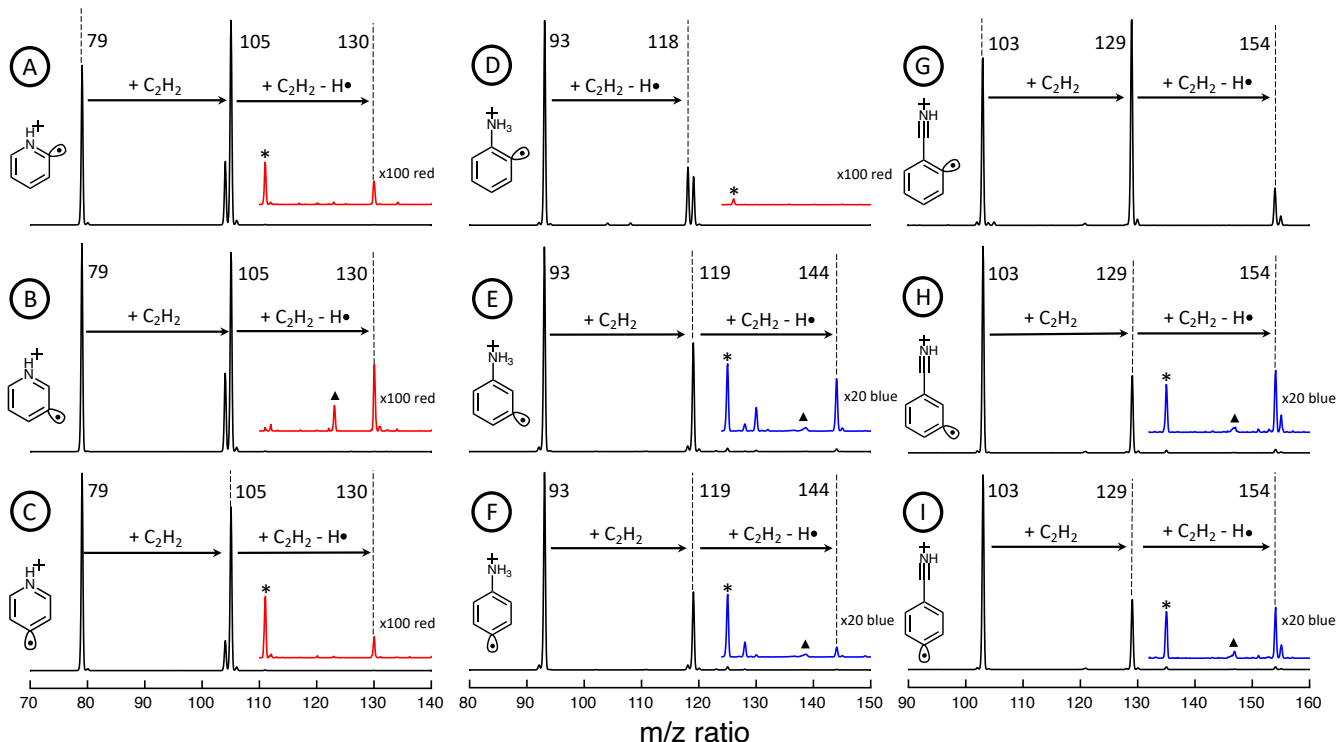
Figure 2. Representative mass spectra for the reactions of acetylene with (A) 2Pyr, (B) 3Pyr, (C) 4Pyr, (D) 2Anl, (E) 3Anl, (F) 4Anl, (G) 2Bzn, (H) 3Bzn, (I) 4Bzn. Product peaks associated with ambient O_2 or H_2O addition are labelled with * and ▲ symbols, respectively.

Results and Discussion

Mass Spectrometry

The $[P + H]^+$ ions formed from the precursors, 2-, 3-, 4-iodopyridine (m/z 206); 2-, 3-, 4-iodoaniline (m/z 220); and 2-, 3, 4-iodobenzonitrile (m/z 230), were each isolated in the ion-trap and irradiated with a single laser pulse at 266 nm leading to the formation of $[P + H - I]^{\bullet+}$ product ions at m/z 79, m/z 93 or m/z 103, respectively. These ions are the σ-type distonic radical cations targeted in this study and are herein referred to as 2Pyr (2-dehydropyrininium, m/z 79), 3Pyr (3-dehydropyrininium, m/z 79), 4Pyr (4-dehydropyrininium, m/z 79), 2Anl (2-dehydroanilinium, m/z 93), 3Anl (3-dehydroanilinium, m/z 93), 4Anl (4-dehydroanilinium, m/z 93), 2Bzn (2-dehydrobenzonitrilium, m/z 103), 3Bzn (3-dehydrobenzonitrilium, m/z 103) and 4Bzn (4-dehydrobenzonitrilium, m/z 103) radical cations. As previously reported, isomerisation between these nine radical cations is negligible under the experimental conditions due to large potential energy barriers for hydrogen atom migration.[29-36] For the Anl radicals however, appreciable population of unreactive ions at m/z 93 are also detected, especially in the 2Anl case. This unreactive ion population is attributed to formation of the conventional radical cation along with the target distonic radical ions (as noted in Ref [31]) and its origins will be discussed in further detail below.

Representative mass spectra for each reaction are shown in Figure 2. In this section, reaction products for Pyr Fig. 2(A-C) reactions will be first discussed before those of Anl Fig. 2(D-F), and then Bzn Fig. 2(G-I). For some target reactions, product ions consistent with secondary acetylene addition are observed. While these secondary reactions are accounted for in the kinetic analysis shown later, these chemistries are beyond the scope of the current paper and will be the subject of a future publication.

Dehydropyridinium (Pyr) Products (m/z 79)

Across all Pyr reactions with acetylene (Fig. 2A, 2B and 2C), the major product peak corresponds to the initial acetylene adduct at m/z 105 $[M + 26]^+$. Signal at m/z 104 is assigned as the H-atom loss co-product ion following formation of the initial adduct $[M + 26 – 1]^+$. The minor product peak at m/z 130 is assigned as the addition of a second acetylene molecule, to the adduct at m/z 105, followed by the loss of a H-atom $[M + 26 + 26 – 1]^+$. The minor peak at m/z 111 is consistent with the addition of background O_2 to the target cation $[M + 32]^+$ and has been previously reported.[29] The peak at m/z 123, observed for reactions with 3Pyr, is assigned as the addition of H_2O to the adduct at m/z 105 $[M + 26 + 18]^+$.

Dehydroanilinium (Anl) Products (m/z 93)

For the three Anl reactions with acetylene (Fig. 2D, 2E and 2F), a major product peak is observed at m/z 119 corresponding to the formation of the first acetylene adduct $[M + 26]^+$. A strong m/z 118 signal, unique to 2Anl, is assigned as H-atom loss from the adduct $[M + 26 - 1]^+$. The equivalent m/z 118 signal is weak for 3Anl and 4Anl. The 3Anl and 4Anl reactions show a peak at m/z 144 (when magnified ×20), which is assigned as H-atom loss following the addition of two acetylene molecules $[M + 26 + 26 – 1]^+$. Another minor peak at m/z 125 corresponds to background O_2 addition to the radical cation, which has been reported previously.[30,36]

Dehydrobenzonitrilium (Bzn) Products (m/z 103)

For Bzn reactions with acetylene (Fig. 2G, 2H and 2I) signal at m/z 129 is assigned as formation of the initial acetylene adduct $[M + 26]^+$ and is the major product across all cases. In contrast to the other systems, signal arising from H-atom loss from this adduct (m/z 128) is not detected for any dehydrobenzonitrilium radical cation. Signal at m/z 154 is
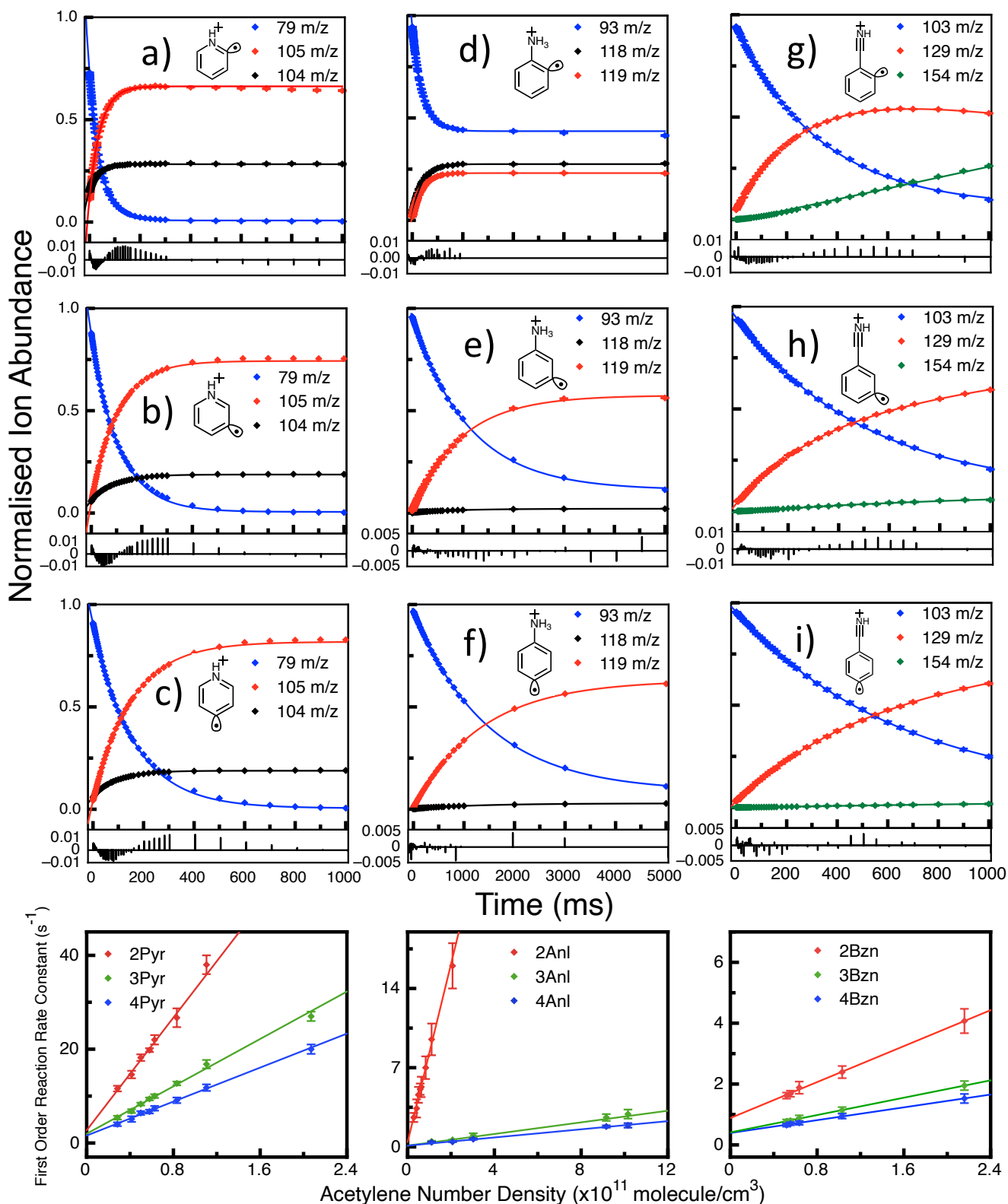
3

Figure 3. Representative kinetic profiles for the reaction of each target radical and acetylene. Acetylene concentrations for kinetic profiles are 8.31×10^{10} molecule cm^{-3} (2Pyr, 3Pyr, 4Pyr, 2Anl), 9.16×10^{11} molecule cm^{-3} (3Anl, 4Anl) and 5.54×10^{10} molecule cm^{-3} (2Bzn, 3Bzn, 4Bzn). Residuals (difference between fitted functions and experimental data) for the decay of each target radical are displayed below each kinetic plot. Plots of first-order reaction coefficients vs acetylene number density, used to extract second-order rate coefficients, are also included. Error bars for these plots represent 2σ.

4

present, corresponding to H-atom loss following the addition of a second acetylene molecule to the first adduct $[M + 26 + 26 – 1]^+$. The m/z 154 product signal is particularly strong for the 2Bzn reaction. Also, present for reactions with Bnz is a minor product peak at m/z 155, assigned as the addition of a second acetylene to the initial adduct $[M + 26 + 26]^+$. Similar to the other reactions, an O_2 addition reaction is also observed, in this case at m/z 135 $[M + 32]^+$.[31]

Reaction Kinetics

Product mass spectra for the reactions of each target radical cation with acetylene were recorded as a function of ion trap storage time across a range of at least five acetylene concentrations. Representative kinetic profiles for the major ions are shown in Figure 3(a-i). The signal of the target radical was fitted with a single exponential decay function to extract the *pseudo*-first-order rate coefficient, at each acetylene concentration. These first-order rate coefficients were then plotted against the acetylene number density within the ion trap and fitted by linear regression (lower panels in Figure 3). The slope of this fitted line corresponds to the second-order rate coefficient. Figure 4 shows the measured second-order rate coefficients for each of the target radical ions reacting with acetylene. Reaction efficiencies were calculated by normalising each second-order rate coefficient to the theoretical Langevin collision rate[37] and they range from 0.2 % for 4Anl up to 37% for 2Pyr, all measured second-order rate coefficients and reaction efficiencies are provided in Table S1 (Supporting Information).
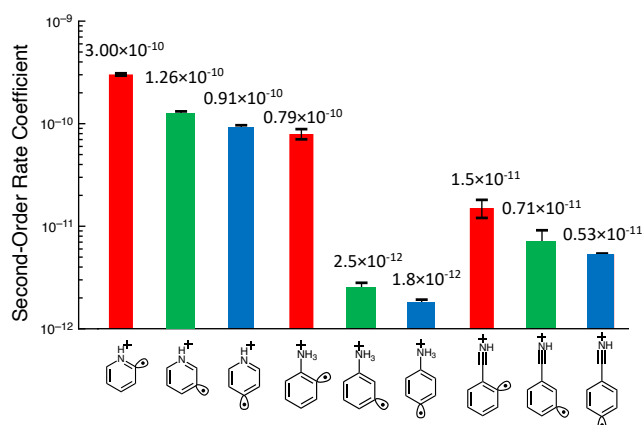

Figure 4. Second order rate coefficients for each target radical reacting with C_2H_2 as determined in this study. Units are cm^3 molecule^{-1} s^{-1} and error bars represent 2σ.

Three observations are noted from the second-order reaction rate coefficients assembled in Figure 4: (i) rate coefficients increase from *para* to *ortho* positions in each set; (ii) second-order rate coefficients can be sorted into three groups; low: between $1–3 \times 10^{-12}$ cm^3 molecule^{-1} s^{-1} (3Anl and 4Anl), intermediate: between $5–15 \times 10^{-12}$ cm^3 molecule^{-1} s^{-1} (2Bzn, 3Bzn and 4Bzn) and high: between $8–31 \times 10^{-11}$ cm^3 molecule^{-1} s^{-1} (2Anl, 2Pyr, 3Pyr and 4Pyr); and (iii) 2Anl is the only radical cation with a second-order rate coefficient distinctly different to its isomers. A rationale for these observations will be developed further below.

Product branching ratios for each reaction are derived by taking the asymptotic limit for the single or biexponential function used to fit the kinetic profiles for each product channel. Table S1 also contains these branching ratios for the major product ions. As mentioned above, although most of the target

radical ion populations react to baseline over the course of experimental time window, the radical ion signal for 2Anl, and to a lesser extent also for 3Anl and 4Anl, does not reach zero intensity. This remaining ion population is attributed to the presence of the unreactive conventional anilinium radical cation (*i.e.*, where the radical and charge are both formally assigned to nitrogen). An explanation for this secondary radical population is due to isomerisation within the short timescale following 2Anl formation. The 266 nm photolysis of the aryl-iodine bond in the iodoaninlinium precursor ion leaves approximately 40.5 kcal/mol of residual energy,[38] which is close to the predicted activation energy for hydrogen atom transfer and isomerisation of 2Anl to the conventional radical ion (E_a = 42 kcal/mol).[31] Thus, isomerisation of 2Anl prior to collisional deactivation by the helium buffer gas may result in the formation of the conventional radical. Other studies have suggested protonation isomers may also provide a source of the conventional radical ion.[39] In either case, as the conventional radical is several orders of magnitude less reactive than the target σ-type distonic radical it is considered unreactive under these timescales investigated here and does not impact on the kinetic analysis of the target distonic radical ion species.

A major difference in branching ratios across all reactions is the amount of signal corresponding to acetylene addition followed by hydrogen atom elimination (m/z 103 Pyr, m/z 118 Anl, m/z 128 Bzn). Reactions of 2Pyr, 3Pyr, 4Pyr and 2Anl all exhibit significantly higher branching ratios for this product channel compared to 3Anl, 4Anl, 2Bzn, 3Bzn and 4Bzn, providing a useful experimental observation to assess the calculated energy schemes in the next section.

Potential Energy Schemes

To determine the important mechanistic pathways and assign products for each reaction, a potential energy scheme for the reaction of each radical ion with acetylene was computed and the results are shown in Figures 5, 6 and 7. Reaction energies were calculated using the composite G3X-K method and values are reported in kcal/mol, relative to the separated reactants. Due to mechanistic similarities between *meta* and *para* reactions, only *para* and *ortho* target radical reactions will be discussed here, however expanded reaction surfaces (including *cis/trans* isomerisation) for both *ortho* and *meta* target radicals are provided in the supplementary information (Figures S1-3). This section will first discuss the reaction pathways of acetylene with 2Pyr and 4Pyr, followed by the reactions of acetylene with 2Bzn and 4Bzn and finally the reactions of acetylene with 2Anl and 4Anl. For each reaction, a pre-reactive complex (PRC) was located, which is crucial to the bimolecular reaction kinetics, and this is investigated in the subsequent section. After forming of the C–C addition bond, the following energy schemes provide information for rationalising the detected product ions and branching fractions. As already noted, only products from the addition of the first acetylene molecule will be discussed here, products associated with secondary acetylene addition to each radical ion will be the subject of a future publication.

Dehydropyridinium Reactions with Acetylene

Following the scheme in Figure 5A, the reaction of 2Pyr with acetylene leads to the formation of **2Pyr$_0$** at –48.2 kcal/mol. From **2Pyr$_0$**, direct H-atom loss from the benzylic position leads to the formation of 2-ethynylpyridinium with a transition state at –11.7 kcal/mol making this the lowest energy pathway for direct H-atom loss across all systems and consistent with the abundant H-atom loss product (m/z 104) for 2Pyr + C_2H_2.

5

Alternatively, from **2Pyr0** a 1,2-H atom shift can occur (–10.5 kcal/mol barrier), leading to the formation of the resonance-stabilised radical **2Pyr1** at –60.1 kcal/mol (11.9 kcal/mol below **2Pyr0**). This intermediate can undergo H-atom loss to form 2-ethynylpyridinium *via* a relatively late transition state at –11.3 kcal/mol. An alternative pathway to form **2Pyr1** from **2Pyr0** requires first forming **2Pyr3**. Although the transition state to form **2Pyr3** is significantly lower in energy than the transition state to form **2Pyr4** directly (–28.4 versus –11.7 kcal/mol), the second transition state along this pathway is notably higher at –9.3 kcal/mol thus diminishing its competitiveness. It is likely that the residual signal detected at *m/z* 105 in Fig. 1A is a mixture of **2Pyr0**, **2Pyr2**, **2Pyr3** and **2Pyr4**. Each of these intermediates are relatively stable with large barriers to isomerisation, increasing their propensity for collisional stabilisation by the buffer gas (on the microsecond timescale).

The energy scheme for 4Pyr (Fig. 5B) describes similar pathways to 2Pyr although due to the location of the *para*-radical site there is no *N*-centred radical intermediate present in this scheme. Addition of acetylene leads to the formation of the intermediate **4Pyr0**, whereby direct H-atom loss forms 4-ethynylpyridinium *via* a –8.9 kcal/mol transition state, which is marginally higher in energy than the corresponding pathway for 2Pyr at –11.7 kcal/mol (*cf*. Fig. 5A). However, formation of the resonance stabilised radical **4Pyr1** is also accessible, proceeding *via* a –12.7 kcal/mol transition state. H-atom loss from **4Pyr1** then proceeds *via* a –8.8 kcal/mol transition state (also higher than the corresponding state for 2Pyr). These two marginally higher energy H-atom loss transition states can explain the lower H-atom loss product yield observed for 4Pyr compared with 2Pyr. From similar arguments as above, we attribute the residual signal at *m/z* 105 as resulting from collisional stabilisation of **4Pyr0**, **4Pyr1** and **4Pyr2**.

However, it is likely both of these pathways will be uncompetitive compared to the two available cyclisation reactions. From **2Bzn0**, an almost negligible barrier leads to a five-membered ring intermediate **2Bzn3** at –77.5 kcal/mol. Also, an alternative six-membered ring closure mechanism can produce the even more stable quinoline species **2Bzn4** at –84.9 kcal/mol. Due to the particularly low barriers for both of these cyclisation mechanisms, rates of formation are expected to be orders of magnitude larger than other pathways. Furthermore, due to deep potential wells for these bicyclic species, back-reaction rates will be meagre, thus these intermediates will comprise a large portion of the ion population. No energetically accessible H-atom loss pathways were identified from either **2Bzn2** or **2Bzn3**. These favourable cyclisation pathways are in accord with the experiments where no H-atom loss products (*m/z* 128) are recorded and therefore prevailing signal at *m/z* 129 is assigned to collisionally stabilised **2Bzn3** and **2Bzn4**. Presumably, it is these intermediates that react with a second C2H2 facilitating higher-order molecular weight growth.

Figure 6B shows the stationary points for the 4Bzn + C2H2 reaction and this follows the same general reaction pathways as 2Bzn but without any bicyclic structures. Pathways to 4-ethylbenzonitrilium + H form *via* a –3.7 kcal/mol transition state from **4Bzn0** or *via* a –7.2 kcal/mol transition state from **4Bzn1**. This aligns with the experimental observation whereby 4Bzn + acetylene reactions produce significantly lower H-atom loss product compared to 4Pyr reactions. Unreactive signal at *m/z* 129 is assigned to collisionally-stabilised intermediates, likely comprising a mixture of **4Bzn0**, **4Bzn1** and **4Bzn2**.
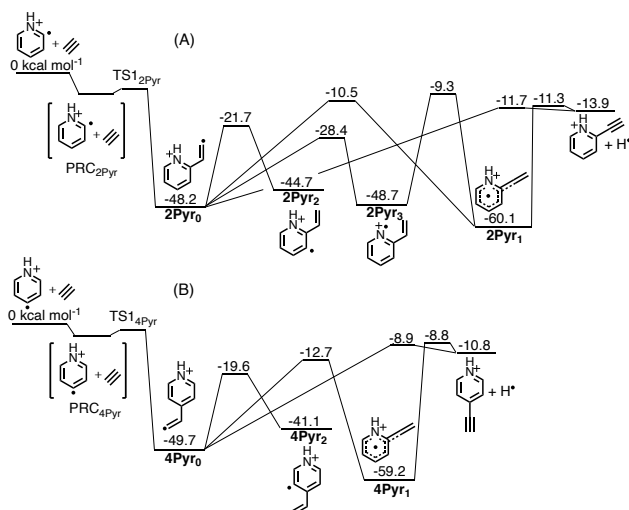

Figure 5. Potential energy schemes for the reactions of acetylene with (A) 2Pyr and (B) 4Pyr. G3X-K energies (kcal/mol) are reported relative to separated reactants.
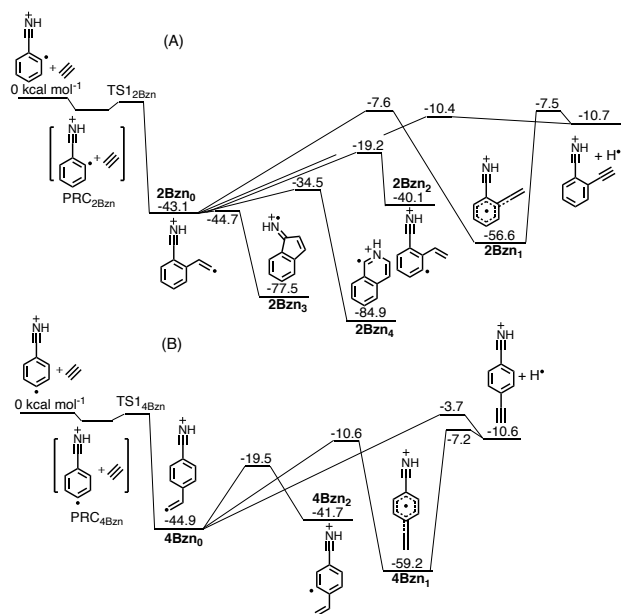

Figure 6. Potential energy schemes for the reactions of acetylene with (a) 2Bzn and (b) 4Bzn. G3X-K energies (kcal/mol) are reported relative to separated reactants.

Dehydrobenzonitrilium (Bzn) Reactions with Acetylene

Figure 6A shows the calculated stationary points for the 2Bzn + C2H2 reaction. Acetylene addition forms the initial adduct **2Bzn0** at –43.1 kcal/mol where H-atom loss can form 2-ethynylbenzonitrilium *via* a late –10.4 kcal/mol transition state. Alternatively, a 1,2-H atom shift forms **2Bzn1**, which can undergo H-atom loss to also yield 2-ethylbenzonitrilium.

Dehydroanilinium (Anl) Reactions with Acetylene

Stationary points for the 2Anl + C2H2 reaction are shown in Figure 7A. Following addition, H-atom loss from **2Anl0** leads to the formation of 2-ethynylanilinium *via* a –7.6 kcal/mol transition state. Alternatively, a 1,2-H atom shift from **2Anl0** leads to a resonance stabilised radical intermediate **2Anl1**. Two

6

H-atom loss channels from **2Anl₁** can proceed producing either 2-ethynylanilinium or **2Anl_p1**. Transition states for these loss channels reside at –10.3 kcal/mol (to 2-ethynylanilinium + H) and –7.3 kcal/mol (to **2Anl_p1** + H). However, neither of these H-atom loss pathways are expected to be major contributors to the H-atom loss product signal at m/z 118, instead, a third mechanism, unique to the 2Anl system, is expected to dominate. This pathway follows a low barrier (4.0 kcal/mol) 1,5-H atom transfer pathway from the -NH₃⁺ substituent to form **2Anl₃**, followed by cyclisation over a very low barrier (0.8 kcal/mol) to produce **2Anl₄**. H-atom loss from **2Anl₄** yields the bicyclic product **2Anl_p2** *via* a –33.0 kcal/mol transition state. Since this pathway is unique to 2Anl, it explains the high yield of m/z 118 in Fig. 1D compared with the 3Anl and 4Anl cases (Fig 1E,F). Product signal at m/z 119 is assigned as collisionally stabilised intermediates, likely **2Anl₃** and **2Anl₄**, due to low formation barriers and increased stabilisation energies.

Stationary points for the 4Anl + C_2H_2 reaction are shown in Figure 7B. With the exception of absent bicyclic species, 4Anl + C_2H_2 follow similar reaction steps as 2Anl. From the initial adduct (**4Anl₀**), direct H-atom loss forms 4-ethylanillinium + H *via* a –3.4 kcal/mol transition state. Alternatively, a 1,2-H atom shift leads to the resonance stabilised radical **4Anl₁**, which can then undergo two H-atom loss channels – one from either end – forming 4-ethylanillinium + H or **4Anl_p1** + H. Residual ion populations at m/z 119 are assigned as collisionally stabilised adducts; likely candidates are **4AnI₀**, **4AnI₁** and **4AnI₂**.
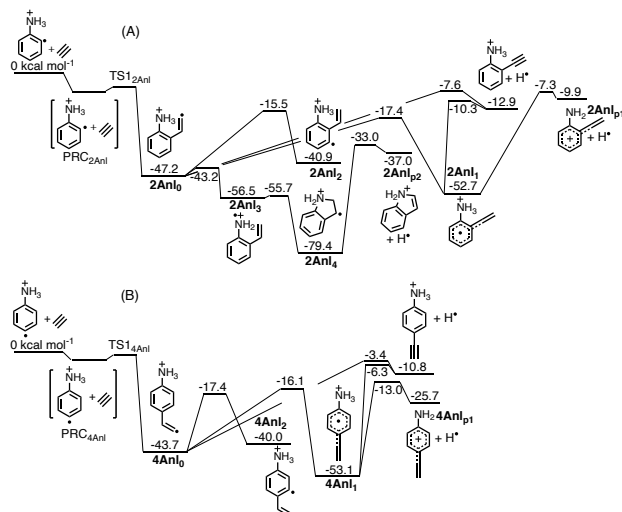

Figure 7. Potential energy schemes for the reactions of acetylene with (A) 2Anl and (B) 4Anl. G3X-K energies (kcal/mol) are reported relative to separated reactants.

Pre-Reactive Complexes and a Kinetic Model

Although these energy schemes provide insight into the detected product ions and product branching ratios, they do not readily assist with explaining the different bimolecular reaction kinetics observed for these reactions. Since all reactions have significantly exothermic addition pathways, and both reaction and product formation rates are essentially matched for each reaction, this points to a decisive kinetic bottleneck along the early stages of the reaction pathway.[40] As outlined in this section, it is possible to rationalise the kinetic trends of each target radical by considering the forward barrier to acetylene addition following the formation of a pre-reactive complex. A generalised scheme showing the key aspects of the pre-reactive complex formation and fate for 2Pyr + C_2H_2 is shown in Fig 8,

including a forward barrier to acetylene addition (relative barrier energy) – which is below the energy of the separated reactants.
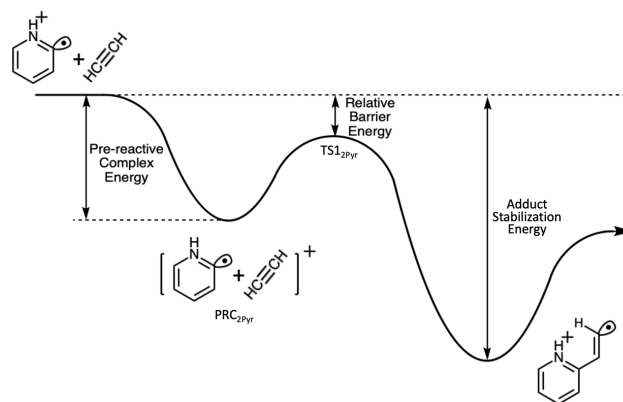

Figure 8: Schematic of the key regions of the potential energy scheme for the reaction between 2Pyr and C_2H_2. All other target reactions follow the same general mechanism.

Quantum chemical calculations for the entrance channel of each target radical encountering C_2H_2 were performed using M06-2X-D3(0)/6-31++G(2df,p) optimised geometries followed by DSD-PBEP86-NL/aug-cc-pVQZ single point energies. For all reactions, pre-reactive complexes were optimised along the addition coordinate of the approaching acetylene. The forward barriers, separating the pre-reactive complex and the adduct, were in most cases below the energy of separated reactants – a case sometimes referred to as a *submerged* barrier.[42,43] This early portion of the potential energy scheme for each reaction is shown in Figure 9a that only includes the energies of the pre-reactive complex (PRC) and the forward barrier to acetylene addition, relative to the energy of the free reactants. The ordering of the forward barrier-energy is the same as the ordering of the experimental second-order reaction coefficients except that 4Pyr and 2Anl are swapped. It is notable that, with the exception of 3Anl and 4Anl, all stationary points lie below the energy of the separated reactants. Also plotted is the reaction efficiency for each target reaction against the relative barrier height for acetylene addition in Figure 9b (logarithmic scale). This general linear trend provides supporting evidence for a dependency between the forward barrier-energies and the overall reaction efficiency. This plot is in accord with the major trends discussed above with: (i) relative barrier heights increasing from *ortho* to *para*, (ii) three groupings existing depending on their barrier height and (iii) the increased second-order rate coefficient of 2Anl. The 2Anl reactivity is captured by its EA value since it fits reasonably well to the trend in Figure 9b but also it does have a notably deeper PRC well at –9.1 kcal/mol. This could be due to some stabilisation from stronger interactions between the acetylene and the -NH₃⁺ group. All PRC structures and the structures of the forward transition state from the PRC are provided in supporting information.

As suggested by ionic curve crossing models, these results can be rationalised by considering the polarization of the initial transition state as dependant on the radical electron affinity (EA) and the ionization energy (IE) of the neutral reagent.[14,17] Therefore, since neutral acetylene is the comment reactant, increasing the radical-ion EA is expected to increase the efficiency of reaction by lowering the key pre-reactive complex forward barrier. The adiabatic EA for each reactant is plotted against the relative barrier height as shown in Figure 9c,

revealing a strong relation between these two parameters. These results indicate that by simply altering the reactant's electron affinity, either by modifying the distance between the radical site and the charged moiety or introducing substituents, the overall reaction efficiency can be predicted for these addition reactions – as least relative to similar reactants.[42]

Furthermore, the IE of the neutral reactant is expected to influence the polarizability at the transition state, with lower ionisation energies corresponding to faster bimolecular kinetics.[17,18] As all reactions here are with acetylene (and thus the ionisation energy remains constant) this effect is not probed, however, our previously reported reactions of the Pyr and Anl distonic radical cations with propene,[29,30] which has a significantly lower ionisation potential compared to acetylene (IE 9.73 eV for propene[44] compared to 11.4 eV for acetylene[45]), show significantly increased reaction efficiencies, up to *ca.* 70%. Another study reported on Bzn + ethylene (IE 10.51 eV for ethylene[46]) and these efficiencies also conform with the trend,[32] and all are included in Figure 9d where the reaction efficiency of now 18 reactions are plotted against the IE – EA energy. In agreement with the ionic curve crossing model, a good correlation between these parameters is obtained until an IE – EA value of roughly less than 3.5 eV, where reactions approach 100% efficiency.[14,17]

The trend is rather good considering the simplicity of the model (with only enthalpic changes considered). There is some scatter in these data with dehydropyridinium + C_2H_2 reactions slightly off the main trend, along with the 2-dehyodraniliunium + C_2H_2 result, but more points are required to better understand the overall trends under this simple relationship. The success of this model indicates that once the PRC forward barrier is crossed, and the C–C addition bond is formed, no reverse reaction occurs. Finally, double-well reactions that proceed from a PRC with barriers below the energy of the reactants are known to be efficient down to even ultracold temperatures – indeed, they tend to demonstrate negative temperature behaviour that results in reaction rates increasing as temperature decreases. Therefor the reactions studied here with forward barriers well below zero are expected to be rapid under extra-terrestrial conditions.

Conclusion

Mass spectrometric product detection experiments, using a modified linear quadrupole ion-trap, were conducted for the gas-phase reactions of acetylene with nine target *N*-protonated aromatic radical cations at room temperature and 2.5 mTorr. Reaction efficiencies were modelled using the relative barrier energy which shows some correlation for each target radical and were linked to the electron affinity of the charged reactant. Comparisons, also including previously reported kinetic data, indicate that reaction efficiencies increase as the difference between the IE of the neutral reactant and the EA of the distonic radical cation decrease. These results are consistent with predictions based on ionic curve crossing model and suggest that the overall reaction efficiency can be tuned by altering either parameter.

Across all reactions, four major product channels were observed corresponding to initial acetylene addition $[M + 26]^+$, H-atom loss from the initial acetylene adduct $[M + 26 - 1]^+$, secondary acetylene addition $[M + 26 + 26]^+$ and H-atom loss from the secondary acetylene adduct $[M + 26 + 26 - 1]^+$. Quantum chemical calculations were used in conjunction with experimental branching ratios to elucidate major products formed from each reaction system. Reactions with *ortho* radical isomers proceeded through markedly different reaction pathways, due to interactions with the adjacent charge centres not available to the *meta* or *para* isomers. For 2Bzn and 2Anl reactions in particular, ring closure mechanisms – forming bicyclic products – from interactions with charged substituents could be relevant to PAH/NPAH growth mechanisms in low temperature environments. Future studies investigating the reactions of each target radical with other small hydrocarbons will assist in developing the theoretical framework necessary to accurately model these reactions across the wide range of temperatures and pressure relevant to combustion, atmospheric and interstellar models. However, other studies, particularly on the molecular weight growth of larger nitrogen-containing aromatic hydrocarbons or secondary addition mechanisms, should be performed to help advance our understanding on the growth of larger NPAH molecules.
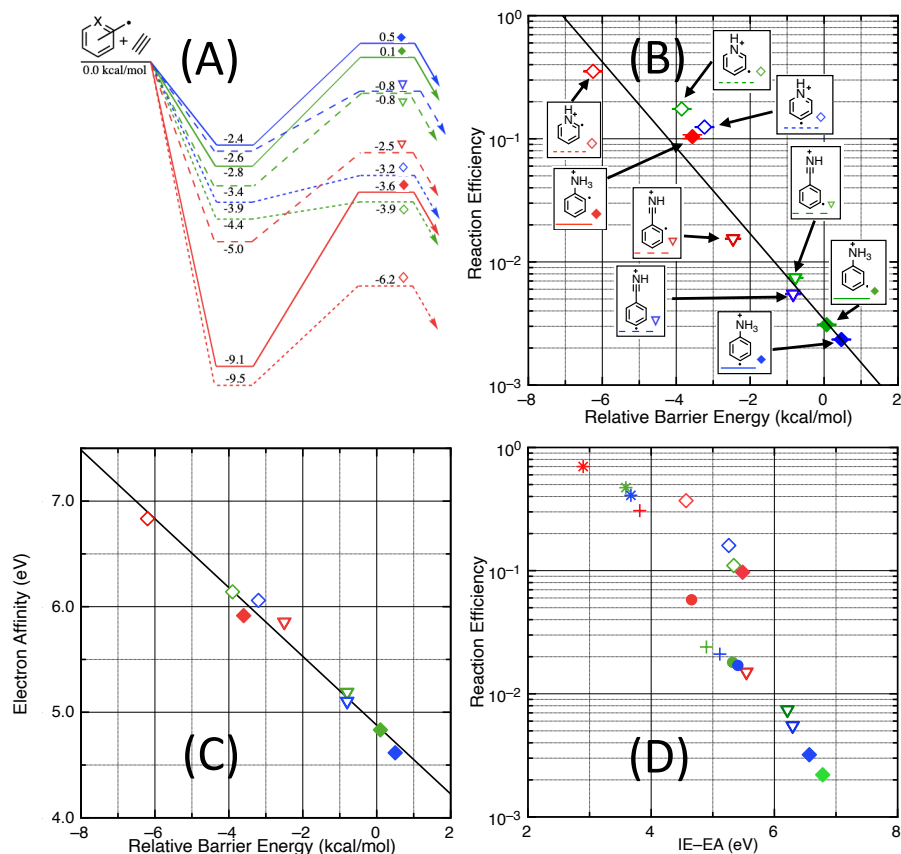
Figure 9: (A) The potential energy surface of the pre-reactive complex for each target radical. DSD-PBEP86-NL/aug-cc-pVQZ//M06-2X-D3(0)/6-31++G(2df,p) energies are given in kcal/mol relative to reactants. (B) Logarithmically scaled plot of reaction efficiency against the forward barrier energy for each target radical. An exponential fit, displayed as a black line, demonstrates a correlation between these two parameters. (C) Plot of relative barrier energies for each reaction and the electron affinity of the corresponding radical cation. (D) Logarithmically scaled plot of the reaction efficiency against IE - EA energy in eV. Reaction efficiencies for Pyr + propene (represented by *) are taken from ref 30, Anl + propene (represented by $^+$) are taken from ref 31 and Bzn + ethylene (represented by •) are taken from ref 32 (the red (*ortho*), green (*meta*), blue (*para*) colouring is consist for each radicals isomer in each set).

ASSOCIATED CONTENT

Supporting Information

The following Supporting Information is available free of charge on the ACS Publications website.
Reaction efficiencies, second-order rate coefficients and product branching ratios for each target reaction.
Representative pseudo first-order rate coefficients for major product channels for each target reaction.
Expanded potential energy surfaces for each the ortho and meta radicals. These surfaces include cis/trans isomerization.

AUTHOR INFORMATION

Corresponding Author

Adam J. Trevitt

E-mail: adamt@uow.edu.au **Phone:** +61 2 4221 5545

REFERENCES

1.   Ferguson EE. Ionospheric ion-molecule reaction rates. Reviews of Geophysics. 1967; 5(3):305-27.
2.   Semo NM, Koski WS. Some ion-molecule reactions pertinent to combustion. The Journal of Physical Chemistry. 1984t; 88(22):5320-4.
3.   Calcote HF, Keil DG. Ion-molecule reactions in sooting acetylene-oxygen flames. Combustion and flame. 1988; 74(2):131-46.
4.   Watson WD. Interstellar molecule reactions. Reviews of Modern Physics. 1976; 48(4):513.
5.   Snow TP, Bierbaum VM. Ion Chemistry in the Interstellar Medium. Annual Review Analytical Chemistry. 2008; 1:229-59.
6.   Rowe BR, Marquette JB. CRESU studies of ion/molecule reactions. International Journal of Mass Spectrometry and Ion Processes. 1987; 80:239-54.
7.   Bell MT, P. Softley T. Ultracold molecules and ultracold chemistry. Molecular Physics. 2009; 107(2):99-132.
8.   Olmstead WN, Brauman JI. Gas-phase nucleophilic displacement reactions. Journal of the American Chemical Society. 1977; 99(13):4219-28.
9.   DePuy CH, Gronert S, Mullin A, Bierbaum VM. Gas-phase SN2 and E2 reactions of alkyl halides. Journal of the American Chemical Society. 1990; 112(24):8650-5.
10.   Gronert S. Mass spectrometric studies of organic ion/molecule reactions. Chemical reviews. 2001; 101(2):329-60.

11. Syage JA, Steadman J. Probing double-minima ion-molecule reaction coordinates by photoelectron spectroscopy of clusters: phenol$^{(1+)}$ + ammonia → phenoxyl + ammonium$^{(1+)}$. The Journal of Physical Chemistry. 1992; 96(24):9606-8.

12. Yates BF, Bouma WJ, Radom L. Detection of the prototype phosphonium (CH2PH3), sulfonium (CH2SH2) and chloronium (CH2ClH) ylides by neutralization-reionization mass spectrometry: a theoretical prediction. Journal of the American Chemical Society. 1984; 106(20):5805-8.

13. Stirk KM, Kiminkinen LM, Kenttamaa HI. Ion-molecule reactions of distonic radical cations. Chemical Reviews. 1992; 92(7):1649-65.

14. Williams PE, Jankiewicz BJ, Yang L, Kenttämaa HI. Properties and reactivity of gaseous distonic radical ions with aryl radical sites. Chemical Reviews. 2013; 113(9):6949-85.

15. Donahue NM, Clarke JS, Anderson JG. Predicting Radical−Molecule Barrier Heights: The Role of the Ionic Surface. The Journal of Physical Chemistry A. 1998; 102(22):3923-33.

16. Clarke JS, Rypkema HA, Kroll JH, Donahue NM, Anderson JG. Multiple excited states in a two-state crossing model: Predicting barrier height evolution for H+ alkene addition reactions. The Journal of Physical Chemistry A. 2000; 104(19):4458-68.

17. Jing L, Nash JJ, Kenttämaa HI. Correlation of hydrogen-atom abstraction reaction efficiencies for aryl radicals with their vertical electron affinities and the vertical ionization energies of the hydrogen-atom donors. Journal of the American Chemical Society. 2008; 130(52):17697-709.

18. Adeuya A, Price JM, Jankiewicz BJ, Nash JJ, Kenttämaa HI. Gas-phase reactivity of protonated 2-, 3-, and 4-dehydropyridine radicals toward organic reagents. The Journal of Physical Chemistry A. 2009; 113(49):13663-74.

19. Petzold CJ, Nelson ED, Lardin HA, Kenttämaa HI. Charge-site effects on the radical reactivity of distonic ions. The Journal of Physical Chemistry A. 2002; 106(42):9767-75.

20. Hansen CS, Kirk BB, Blanksby SJ, O'Hair RA, Trevitt AJ. UV photodissociation action spectroscopy of haloanilinium ions in a linear quadrupole ion trap mass spectrometer. Journal of The American Society for Mass Spectrometry. 2013; 24(6):932-40.

21. Hyman MR, Arp DJ. Quantification and removal of some contaminating gases from acetylene used to study gas-utilizing enzymes and microorganisms. Applied and Environmental Microbiology. 1987; 53(2):298-303.

22. Moré JJ. The Levenberg-Marquardt algorithm: implementation and theory. Numerical analysis 1978 (pp. 105-116). Springer, Berlin, Heidelberg.

23. Langevin MP. Une formule fondamentale de théorie cinétique. InAnnales de chimie et de physique, Series 1905 (Vol. 5, pp. 245-288).

24. Cartoni A, Catone D, Bolognesi P, Satta M, Markus P, Avaldi L. HSO2+ Formation from Ion-Molecule Reactions of SO2·+ with Water and Methane: Two Fast Reactions with Reverse Temperature-Dependent Kinetic Trend. Chemistry–A European Journal. 2017; 23(28):6772-80.

25. Hohenstein EG, Chill ST, Sherrill CD. Assessment of the performance of the M05−2X and M06−2X exchange-correlation functionals for noncovalent interactions in biomolecules. Journal of Chemical Theory and Computation. 2008; 4(12):1996-2000.

26. Yu F, Fu LX, Yang Y. DSD-PBEP86-NL and DOD-PBEP86-NL functionals for noncovalent interactions: Basis set effects and tentative applications to large noncovalent systems. International Journal of Quantum Chemistry. 2017; 117(19):e25417.

27. Yu F. Spin-component-scaled double-hybrid density functionals with nonlocal van der Waals correlations for noncovalent interactions. Journal of Chemical Theory and Computation. 2014; 10(10):4400-7.

28. da Silva G. G3X-K theory: A composite theoretical method for thermochemical kinetics. Chemical Physics Letters. 2013; 558:109-13.

29. Bright CC, Prendergast MB, Kelly PD, Bezzina JP, Blanksby SJ, da Silva G, Trevitt AJ. Highly efficient gas-phase reactivity of protonated pyridine radicals with propene. Physical Chemistry Chemical Physics. 2017; 19(46):31072-84.

30. Kelly PD, Bright CC, Blanksby SJ, da Silva G, Trevitt AJ. Molecular Weight Growth in the Gas-Phase Reactions of Dehydroanilinium Radical Cations with Propene. The Journal of Physical Chemistry A. 2019; 123(41):8881-92.

31. Shiels OJ, Kelly PD, Blanksby SJ, da Silva G, Trevitt AJ. Barrierless Reactions of Three Benzonitrile Radical Cations with Ethylene. Australian Journal of Chemistry. 2020.

32. Flammang R, Barbieux-Flammang M, Gualano E, Gerbaux P, Le HT, Nguyen MT, Turecek F, Vivekananda S. Ionized benzonitrile and its distonic isomers in the gas phase. The Journal of Physical Chemistry A. 2001;105(37):8579-87.

33. Lavorato D, Terlouw J, McGibbon G, Dargel T, Koch W, Schwarz H. Generation of neutral and cationic hydrogen shift isomers of pyridine: a combined experimental and computational investigation. International journal of mass spectrometry. 1998 Nov 23;179:7-14.

34. Widjaja F, Jin Z, Nash JJ, Kenttämaa HI. Comparison of the Reactivity of the Three Distonic Isomers of the Pyridine Radical Cation Toward Tetrahydrofuran in Solution and in the Gas Phase. Journal of The American Society for Mass Spectrometry. 2013 Jan 24;24(4):469-80.

35. Rap DB, Marimuthu AN, Redlich B, Brünken S. Stable isomeric structures of the pyridine cation (C5H5N•+) and protonated pyridine (C5H5NH+) elucidated by cold ion infrared spectroscopy. Journal of Molecular Spectroscopy. 2020 Aug 30:111357.

36. Errabelli R, Zheng Z, Attygalle AB. Formation of Protonated ortho-Quinonimide from ortho-Iodoaniline in the Gas Phase by a Molecular-oxygen-mediated, ortho-Isomer-specific Fragmentation Mechanism. Journal of the American Society for Mass Spectrometry. 2020; 31(4):864-72.

37. Langevin MP. Une formule fondamentale de théorie cinétique. Annales de chimie et de physique, Series 1905 (Vol. 5, pp. 245-288).

38. Blanksby SJ, Ellison GB. Bond dissociation energies of organic molecules. Accounts of Chemical Research. 2003; 36(4):255-63.

39. Attygalle AB, Xia H, Pavlov J. Influence of ionization source conditions on the gas-phase protomer distribution of anilinium and related cations. Journal of The American Society for Mass Spectrometry. 2017; 28(8):1575-86.

40. Schmid P, Greenberg J, Nguyen TL, Thorpe J, Catani K, Krohn O, Miller M, Stanton J, Lewandowski H. Isomer-Selected Ion-Molecule Reactions of Acetylene Cations with Propyne and Allene. Physical Chemistry Chemical Physics. 2020.

41. Kaiser RI, Parker DS, Mebel AM. Reaction dynamics in astrochemistry: Low-temperature pathways to polycyclic aromatic hydrocarbons in the interstellar medium. Annual Review of Physical Chemistry. 2015; 66:43-67.

42. Meyer J, Wester R. Ion–molecule reaction dynamics. Annual Review of Physical Chemistry. 2017; 68:333-53.

43. Smith IW, Sage AM, Donahue NM, Herbst E, Quan D. The temperature-dependence of rapid low temperature reactions: experiment, understanding and prediction. Faraday discussions. 2006;133:137-56.

44. Traeger JC. A study of the allyl cation thermochemistry by photoionization mass spectrometry. International Journal of Mass Spectrometry and ion processes. 1984 Jun 8;58:259-71.

45. Plessis P, Marmet P. Electroionization study of acetylene and fragment ions. International Journal of Mass Spectrometry and Ion Processes. 1986; 70(1):23-44.

46. Ohno K, Okamura K, Yamakado H, Hoshino S, Takami T, Yamauchi M. Penning ionization of HCHO, CH2CH2, and CH2CHCHO by collision with He (23S) metastable atoms. The Journal of Physical Chemistry. 1995; 99(39):14247-53.

Second-Order Rate Coefficient

Pre-reactive Complex Energy

Relative Barrier Energy

Adducts

$+ C_2H_2$